Stochastic Nonlinear Analysis of Unidirectional Fiber Composites using Image-based Microstructural Uncertainty Quantification

Tianyu Huang[1], Jiaying Gao[1], Qingping Sun[2], Danielle Zeng[3], Xuming Su[3], Wing Kam Liu[1], Wei Chen[1*]

1. Department of Mechanical Engineering, Northwestern University, Evanston, IL 60208, United States
2. Jiangsu Province Key Laboratory of Aerospace Power System, College of Energy and Power Engineering, Nanjing University of Aeronautics and Astronautics, Nanjing, China
3. Research and Advanced Engineering, Ford Motor Company, Dearborn, MI 48121, United States

* Corresponding author. Email address: weichen@northwestern.edu (W. Chen)

Abstract

We present a data-driven nonlinear uncertainty quantification and propagation framework to study the microstructure-induced stochastic performance of unidirectional (UD) carbon fiber reinforced polymer (CFRP) composites. The proposed approach integrates (1) microscopic image characterization, (2) stochastic microstructure reconstruction, and (3) efficient multiscale finite element simulations enabled by self-consistent clustering (SCA) analysis. To model the complex microstructural variability, the proposed UQ methods take the non-Gaussian uncertainty sources into account through a distribution-free sampling approach leveraging nonparametric and asymptotic statistical tools. A hierarchical conditional sampling strategy enables the simultaneous sampling of multiple sources of uncertainties. Our approach provides insights into the impact of microstructural variabilities, which are shown to have an increasing impact on the nonlinear responses of UD CFRP parts under progressive compression loading and ultimately on the failure rate over time. We discover that before CFRP parts start to fail, a characteristic time period emerges with distinctive uncertainty distributions specific to the microstructure variability and the probability of failure. Identifying the failure time period is crucial to the reliability prediction, which is an essential component of CFRP design.

Keywords. Uncertainty quantification and propagation, image analysis, fiber waviness and nonuniform distribution, efficient multiscale modeling

1. Introduction

Understanding the role of anisotropic microstructures in carbon fiber reinforced polymer (CFRP) composites is critical in its design via integrated computational materials engineering (ICME, [1,2]). A substantial amount of work (e.g. [3–6]) has been undertaken in the digital modeling of CFRP microstructures and predicting the resulting material properties and structural performance via computational methods such as finite element analysis (FEA). On the other hand, local microstructures are not exactly the same everywhere; variations and imperfections in the manufacturing processes lead to spatial microstructure variability [7]. It has been shown [8,9] that ignoring the uncertainties in designing composites structures often results in overestimated reliabilities. Consequently, integrating uncertainty quantification (UQ) into ICME is essential in designing reliable and robust materials and structures [10].

Many studies [10–15] have been conducted to develop UQ and uncertainty propagation (UP) approaches for CFRP. Depending on how the uncertain quantities are represented, UQ methods are broadly categorized as expansion-based or sampling-based. The majority of the former use polynomial chaos expansion (PCE) to decompose the quantity of interests (QoIs) into Hermite polynomials of Gaussian random variables, subsequently leading to the development of theories of stochastic and random field finite elements methods [16–20] for UQ of composites (e.g., [10,21]). However, this approach suffers from the *curse of dimensionality* when the order of expansion and the number of PCE inputs increase. Sampling-based approaches typically utilize Monte Carlo (MC) methods to generate samples as inputs from probability distributions (e.g., Gaussian distribution), then QoIs are evaluated and their moments are computed as estimates of their statistical counterparts (e.g., [22]). In the literature of composite materials UQ, many researchers have developed sampling methods for distributions with a predetermined parametric form. For example, to account for the hierarchical nature of composites, Bostanabad et al. [11] modeled the spatially-varying microstructure and constituent parameters of woven CFRP via Gaussian random fields, and developed a top-down sampling approach to facilitate multiscale simulations and UQ. Naskar et al. [13] combined uniform distributions of material parameters and Gaussian white noises in simulation results to quantify the uncertainties in the natural frequency of composite beams. A review paper [8] summarized widely used statistical models for properties of glass and carbon fiber reinforced composites. However, as the authors of [8] concluded, physical measurements of spatially correlated characterizations of composite materials are lacking. There is a need for sampling approaches to stochastically characterize and generate these random fields.

The computational cost of sampling-based UQ approaches depends on the sample size as well as the time to execute each deterministic model. Hence, to achieve feasible UQ it is crucial to reduce the cost of each deterministic simulation. Although some cost-effective metamodels (e.g., Gaussian process regression [11] or radial basis functions [23]) have been exploited to replace physical simulations, a balance between introduced modeling error and increased efficiency must be reached. For composite structures with microstructure analyses, the Representative Volume Element (RVE) method can provide nonlinear material models with high fidelity predictions, but the rising computational cost of directly simulating RVEs with nonlinear properties (e.g., plasticity and damage) impedes its deployment into multiscale analyses [24–26]. Self-consistent Clustering Analysis (SCA), a data-driven reduced order modeling method, emerged as an alternative to direct numerical simulations of RVEs, reducing the cost of computation by an order of 10^5 with comparable accuracy [27,28]. SCA has been employed for the two-scale concurrent multiscale modeling [29] of CFRP in UD laminate structures.

In this work, we focus on UQ and UP of UD composites with complex microstructural variabilities. In the past, the UD CFRP parts are often assumed to contain straight and uniformly distributed fibers in micro-mechanics analysis of UD CFRP [3,4]. However, optical and CT characterizations [30,31] of the material indicate that manufacturing-induced microstructural irregularities such as wavy and locally aggregated fibers inevitably exist. Further, it has been shown that degraded mechanical properties, for example, Young's modulus and bending strength, should be expected in the presence of fiber waviness [7,32–35], and nonlinear behavior such as local stress and damage initiation, could be altered due to nonuniform fiber distributions [36–41]. However, these prior studies consider only one of the microstructure irregularities at a time in a deterministic fashion. UQ of multiple sources of microstructure variabilities and their compound effect on the structural performance have not been reported.

We propose a data-driven microstructural UQ approach for assessing the impact of complex variability of UD composites on the structural nonlinear performance. The proposed framework consists of three modules: (1) microscopic image characterization, (2) stochastic microstructure reconstruction, and (3) efficient multiscale simulations. Starting with algorithms to extract stochastic microstructure information from images, methods are developed to randomly generate realistic microstructure fields conforming to the image data, which are non-Gaussian, nonstationary, and nonhomogeneous. Furthermore, integrating SCA into multiscale simulations [23, 38] allows us to capture the detailed local UD microstructure evolution in simulating the stochastic CFRP structural nonlinear performance until the point of part failure with a manageable computational complexity.

The rest of the paper is organized as follows. In Sec. 2, we introduce the proposed methods for UQ and UP of realistic UD composites. Sec. 3 describes the UD CFRP case study, including the FEA model and microstructure inputs. The results are analyzed in Sec. 4. We conclude with a summary of contributions and findings in Sec. 5.

2. Methods for Microstructure Characterization and Uncertainty Quantification

In this section, we present the methodological developments for image-based microstructural UQ. For UD fiber composites, a near-orthotropic material, the uncertainties in microstructure can be viewed as the composition of variations from their *cross-sectional* (for the 2D transverse, or *yz*, plane in Fig. 1) and *transverse* (for the 1D longitudinal, or *x*, direction) positions, namely *fiber distribution* and *waviness* (see Fig. 1). The variability is from the nature of the material's manufacturing processes, e.g., imperfect control of the processing environment such as temperature and pressure fields, and it is observed from a set of microscopic images that the distribution is extremely high-dimensional and cannot be explicitly described by parametric distribution functions such as Gaussian distributions.

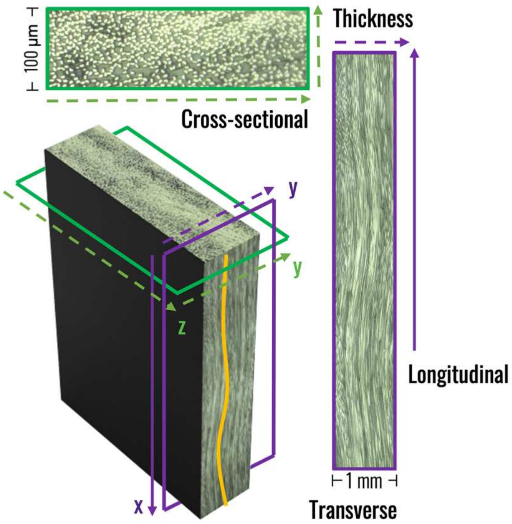

Figure 1. Illustration of the UD fiber composite system with fiber distribution and waviness.

The UQ and UP process is shown in Fig. 2. Since the characterization and stochastic reconstruction of the microscale material geometry are at the core of microstructural UQ [43], we start by characterizing microscopic images and modeling them as realizations of a multivariate random field of fiber distribution and waviness. Second, distribution-free sampling approaches are developed for each microstructure attribute. Next, a hierarchical conditional sampling strategy is proposed to generate the multivariate MC samples of stochastic microstructures. Finally, the samples are passed to the SCA-enabled multiscale simulation program, which efficiently propagates the uncertainty in microstructure to the nonlinear macroscale part performance until failure.

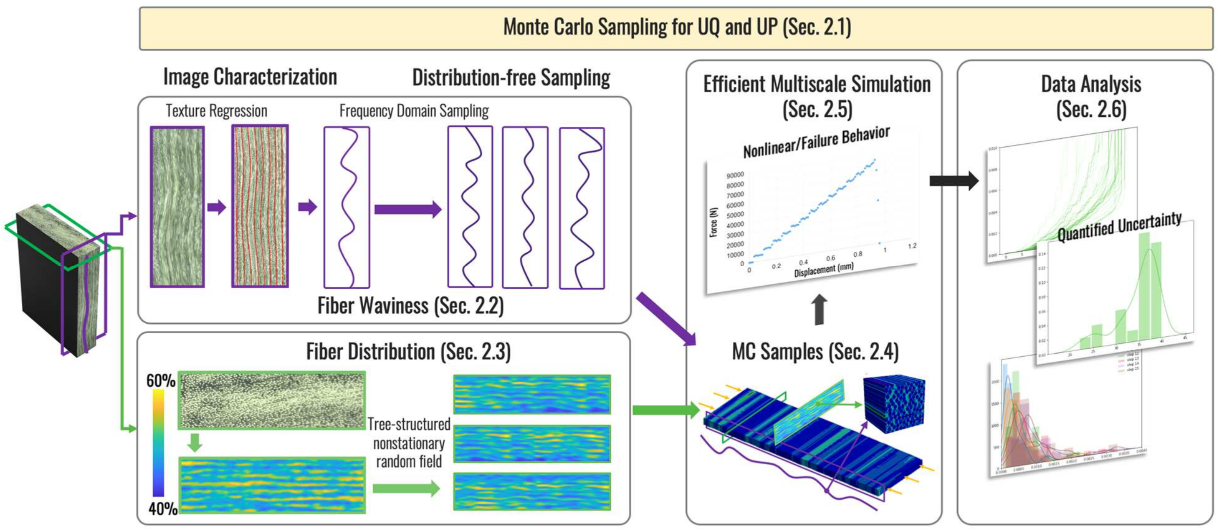

Figure 2. Data-driven uncertainty quantification of UD CFRP composites.

2.1. *Stochastic Microstructure Field and Monte Carlo based UQ and UP*

Let $\mu = \{\mu_{xyz} \in \mathbb{R}^{d_\mu}: (x, y, z) \in \mathbb{R}^3\}$ be a d_μ-dimensional location-indexed microstructure descriptor field, and similarly define a material property field $\rho = \{\rho_{xyz} \in \mathbb{R}^{d_\rho}: (x, y, z) \in \mathbb{R}^3\}$, and a performance metric of interest $\phi = g(\rho, \Omega, \Gamma)$, where Ω represents a part geometry and Γ are boundary conditions and $g(\cdot)$ are typically mechanistic models to be solved numerically. For notational simplicity, we fix Ω and Γ and rewrite $g(\cdot)$ as $\phi = g(\rho; \Omega, \Gamma) \doteq g(\rho)$. Since a material's properties are determined by its microstructure, i.e., $\rho_{xyz} = h(\mu_{xyz})$ or equivalently $\rho = h(\mu)$, where $h(\cdot)$ is an RVE or micromechanics equations, we obtain the deterministic model of microstructure-based mechanical analysis

$$\phi = g(h(\mu)). \tag{1}$$

For UQ, let μ be realizations of a random field M defined by a probability space $\{\mathcal{M}, \mathcal{E}, P_M\}$, where $\mathcal{M} = \{\mu\}$ is the space of stochastic microstructures, $\mathcal{E}$ is the σ-algebra on $\mathcal{M}$, and P_M is the probability measure, $P_M: \mathcal{E} \to [0, 1]$, assigning each event in $\mathcal{E}$ a probability with the constraint $P_M(\mathcal{M}) = \sum P_M(\mu) = 1$. It follows that $\Phi = g\big(h(M)\big)$ is also probabilistic and the purpose of UQ is to obtain the distribution of Φ, $P_\Phi(\cdot)$, when analytical derivation is intractable. Without loss of generality, we assume $\mathcal{M}$, $g(\cdot)$ and $h(\cdot)$ are continuous. Define the density function of microstructures (and performance indicator with Φ and ϕ in subscripts) $f_M: \mathbb{R}^{d_\mu} \to \mathbb{R}_{\geq 0}$ as $P_M(A_\mu) = \int_{A_\mu} \mathrm{d}P_M = \int_{A_\mu} f_M \mathrm{d}\mu$, where A_μ is any measurable subset of $\mathcal{M}$. For independently and identically distributed (i.i.d.) samples $\mu_1, \mu_2, \dots, \mu_n$ from $M_1, M_2, \dots, M_n$, we have

$$\frac{1}{n}\sum_i q\left(g\big(h(\mu_i)\big)\right) \to E_\Phi[q(\Phi)],\ \mu_i \sim f_M(\mu),\ \text{as } n \to \infty, \tag{2}$$

which is the Monte Carlo [12] estimation of the uncertainty of Φ, as $q(\cdot)$ can be carefully chosen to estimate the characteristics of Φ, such as moments and distribution. Each μ_i is called a MC sample. In the following sections, we present our approaches to create i.i.d. microstructure samples with multiple sources of uncertainty from image data, and to evaluate their performance (Eq. (2)) via efficient multiscale simulations.

2.2. *Image-based Distribution-free Sampling of Fiber Waviness*

Fiber waviness from the transverse plane (Fig. 1) is modeled by a stochastic process of local fiber orientations indexed by longitudinal locations. We develop a linear texture image regression algorithm to capture local waviness angles on transverse images. A distribution-free sampling method is then proposed, assuming that (1) fibers share the same waviness profile, and (2) the stochastic process is stationary. These assumptions allow us to utilize the asymptotic properties of stochastic processes to generate random samples.

2.2.1. *Regression of Linear Textures for Waviness Data Extraction*

We define waviness as the collection of fibers' orientations along their longitudinal direction. In optical microscopic images (Fig. 3(a) and (b)), an orientation can be identified visually via the trend of pixels representing fibers, and quantitatively via the angle between the trend and the horizontal axis, as in α in Fig. 3(b). We work with binarized image segments (Fig. 3(c)), each containing a region small enough to enclose an almost linear texture. It follows that the slope of the linear lines (denoted by β) is related to α through $\beta = \tan(\alpha)$.

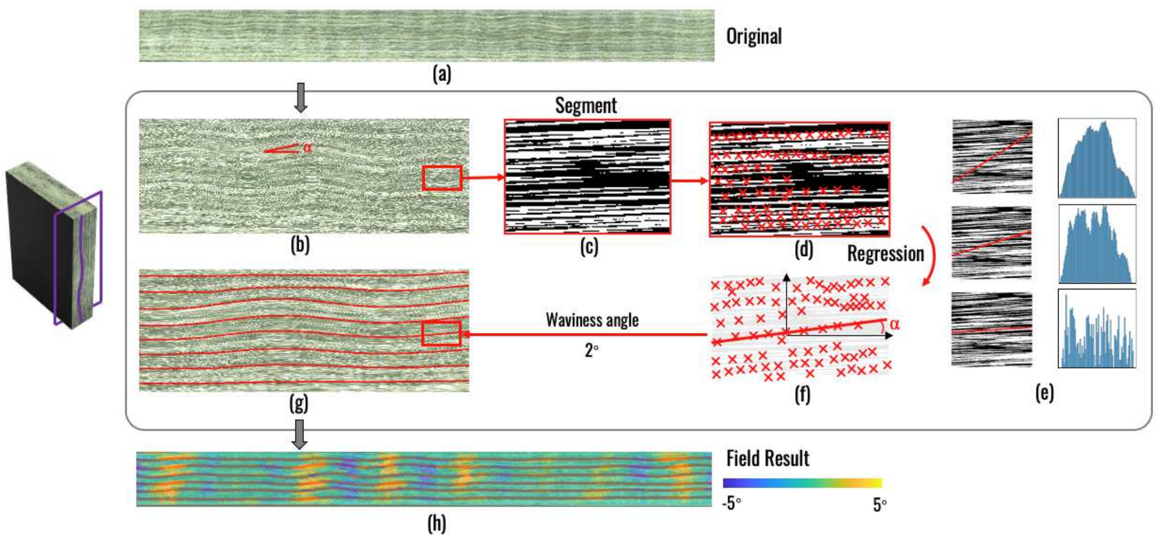

Figure 3. Characterization of transverse images for fiber waviness modeling: (a) a transverse image, (b) a local region with waviness angle shown in red, (c) a binarized segment, (d) fiber pixels marked in red, (e) linear texture regression characterization of the image, (f) regression result, (g) local waviness marked in (b), and (h) characterization results as a waviness field.

Let (X_i, Y_i) be the coordinate of the *i*-th fiber pixel in Fig. 3(d) after binarizing the segments, with linear model $Y_i = \beta X_i + \epsilon_i$ where ϵ_i is a noise term. For linear textures, the points are confined in a rectangular domain, imposing upper and lower bounds on ϵ, and its distribution depends on the placement of fibers. Therefore, the ordinary linear regression, assuming ϵ follows an unbounded zero-mean Gaussian distribution, does not apply.

We propose the *regression of linear textures* (ROLT, Fig. 3(d)-(f)) method for texture regression scenarios. In ROLT, the slope is estimated by

$$\hat{\beta} = \mathrm{argmax}_{\beta} r(e; \beta), \tag{3}$$

where e are the residuals ($e_i = Y_i - \beta X_i$) with the regression line under slope β, $r(\cdot): \mathbb{R}^n \rightarrow \mathbb{Z}^+$(assume there are n points) maps e to the number of modes (roughness) in its probability density estimation (Fig. 3(e), where r increases from top to bottom). The optimization problem (Eq. (3)) works particularly well for capturing the trend of linear textures because if a slope truly represents the fiber orientation, all residuals from the pixels of a single fiber will have the same value and produce an individual peak in the density. A texture of multiple trend lines will result in multiple peaks. An example characterization results are given in Fig. 3 (g) and (h).

2.2.2. *Frequency Domain Sampling for Distribution-free Stochastic Waviness Reconstruction*

As in Fig. 4(a), ROLT quantifies 2D waviness fields from images. Assuming all fibers follow the same waviness profile, we average the field along the thickness direction and obtain a 1D wave (Fig. 4(b)) with spatially varying amplitudes and frequencies, indicating that it is the sum of multiple sine waves. To preserve this feature, the wave's periodogram, the estimate of the spectral density of a 1D time or spatial process, is computed to characterize the wave's features in the frequency domain (Fig. 4(c)). Let $W(k), k = 0,1, \ldots, N$ denote the fiber waviness angle α at location k and $a(\lambda)$ is the discrete Fourier transform (DFT) of $W(k)$ with $\lambda = \frac{2\pi k}{N}$ and $\lambda \in$

$[0,2\pi]$. The periodogram $I(k) = |a(\lambda)|^2, k = 0,1,\dots,N$ (Fig. 4 (c)) of a stationary series, according to [44], converges in distribution to a sequence of independently and *exponentially* distributed random variables as $N \to \infty$.

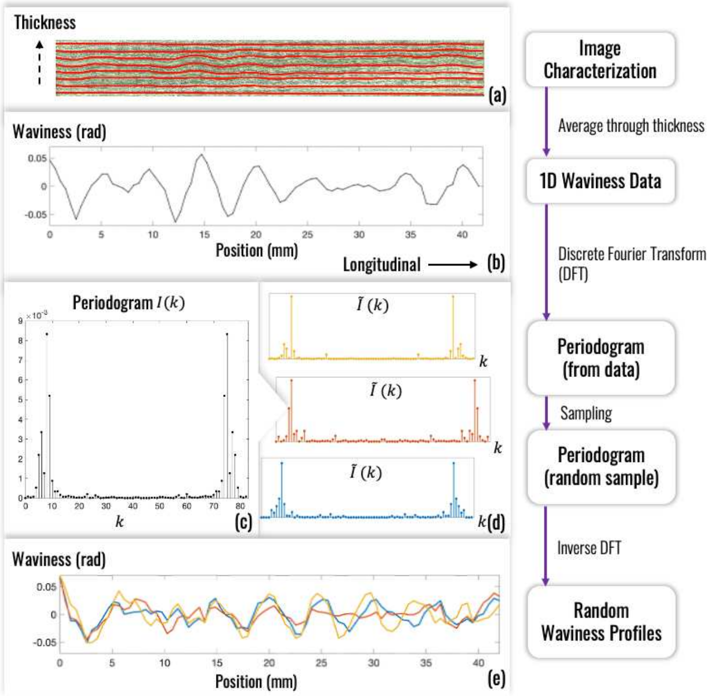

Figure 4. Stochastic reconstruction of fiber waviness: (a) image characterization, (b) 1D waviness signal from averaging (a) through thickness (about 41.5 mm), (c) the periodogram of (b) (83 sampling points), (d) randomly sampled periodograms, and (e) random waviness samples reconstructed from (d).

It follows that the statistical distribution of $I(k)$ is always exponential regardless of how $W(k)$ distributes as long as N is sufficiently large. This property leads to our distribution-free stochastic reconstruction method for general stationary 1D series data by (1) computing its DFT, (2) sampling in the frequency domain from the exponential distributions, and (3) using inverse DFT to convert the sample back to a waviness profile (Fig. 4).

Three stochastic reconstructions are presented in Fig. 4(e). The spatially varying amplitude and wavelength features are well preserved while the randomness is maintained. Note that the proposed method only assumes the 1D data series is stationary and its size is sufficiently large to guarantee the validity of the asymptotic convergence theorem for the periodogram. Although we show its application to a single series, statistical inference methods, such as maximum likelihood estimation, can be adopted to estimate the distribution parameters from multiple data.

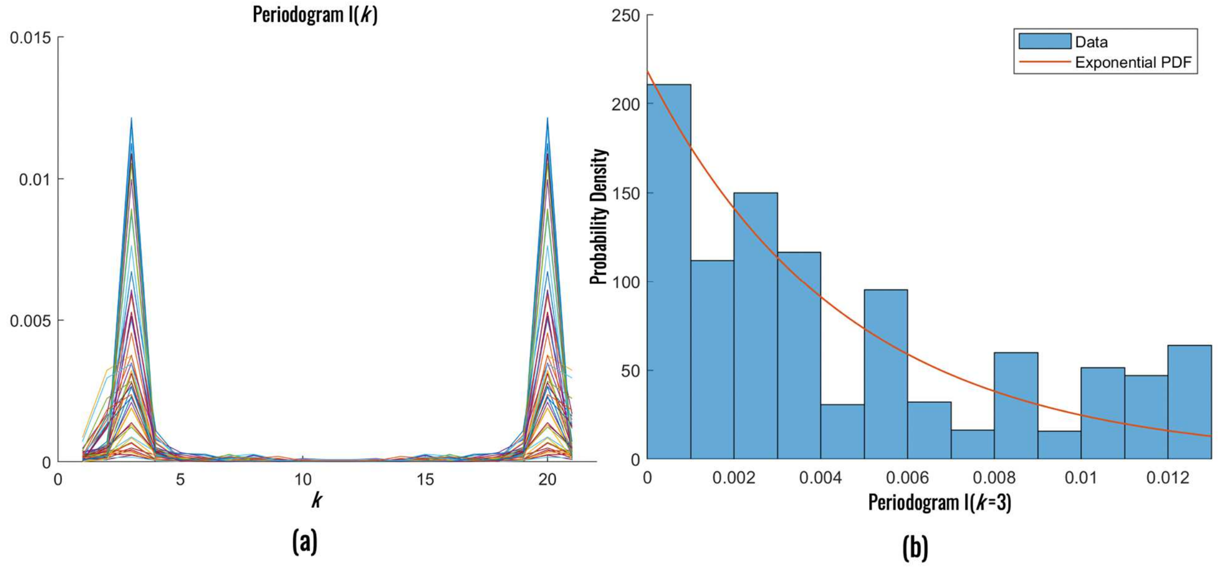

Figure 5. Validation of convergence for data with 21 sampling points. (a) 1000 randomly sampled periodograms. (b) Distribution of $I(3)$ (the peak) and the probability density function of an exponential distribution.

To validate the convergence theorem our approach is based on, we show our data (83 sampling points on a wave of about 41.5 mm) is large enough by demonstrating that even a smaller sample of 21 points is sufficient. The validation is performed on a smaller sample because we can randomly resample from the original data and observe the periodogram's distribution, which should be exponential if the convergence theorem holds. 1000 samples are generated (Fig. 5 (a)) and the histogram of the periodogram's entries show an approximately exponential distribution. The distribution of the 3rd entry, which has the largest amplitude, is given in Fig. 5 (b), along with the exponential distribution with the sample mean as its parameter. It shows the theorem is valid even for a series smaller than our data, and we reason that the convergence theorem can be safely applied in our waviness sampling approach.

The proposed distribution-free reconstruction method also allows us to conduct sensitivity analyses by conveniently changing the magnitudes of the wave's amplitude and wavelength. Let the original data be $W(k)$ and we express the change in amplitude and wavelength as multiples of the original data, for example, 2x amplitude or 0.5x wavelength. To amplify the amplitude by a factor of m, simply multiply the original data $W(k)$ by m ($W(k) \leftarrow m \cdot W(k)$). Similarly, to adjust the wavelength, a transformation of $W(k) \leftarrow W(m \cdot k)$ can be applied with $m \cdot k$ rounded to the nearest integer. For $m > 1$, interpolation is needed to fill any missing integer value between $W(m \cdot k)$ and $W\big(m \cdot (k+1)\big)$. If $m < 1$, a higher resolution signal is obtained (as the interval between points shrinks).

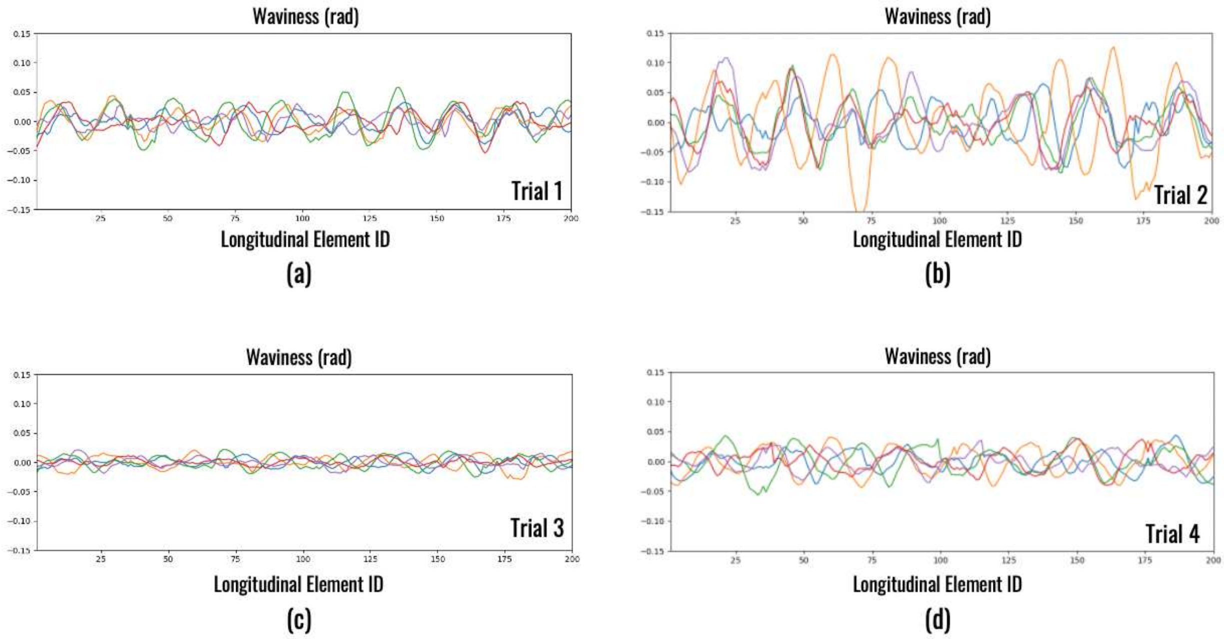

Figure 6. Random realizations of fiber waviness for different scenarios: (a)-(d) represent reconstructions from the (a) original waviness data, (b) 2x the amplitude, (c) 0.5x the amplitude, and (d) 1.25x the wavelength.

Trials on sampling for different waviness profiles are shown in Fig. 6. Each trial contains five (5) realizations. It can be observed that pseudo samples (the realizations) from hypothetical waviness, possessing the original data's stochastic waviness features such as fluctuating amplitudes and wavelengths, can be constructed via the proposed approach.

2.3. *Image-based Distribution-free Sampling of Fiber Distribution*

The distribution of fibers is quantitatively characterized by the location-indexed local volume fractions (denoted by v_{xy}, where (x, y) is the coordinate of a point in the image) by binarizing then locally averaging the cross-sectional microscopic images (Fig. 7). The resulting field of volume fraction shows strong nonhomogeneity, i.e., the layered pattern, and nonstationarity, i.e., the curvature of layers. We assume that the nonhomogeneity is from the nature of its manufacturing process (e.g., molding from a certain number of laminates) and the nonstationarity comes from random variations during the processing. Thus, a nonstationary random field representation would be the most appropriate.

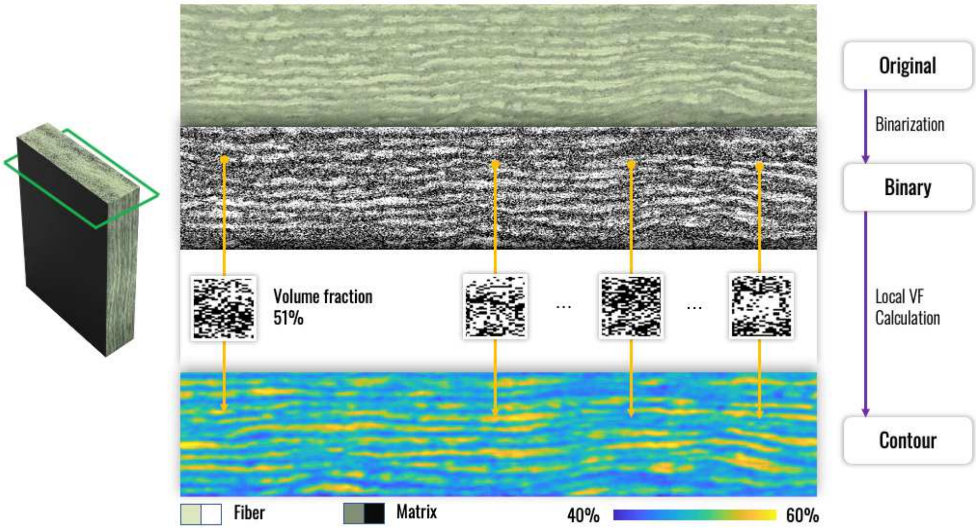

Figure 7. Characterization of cross-sectional images for fiber distribution modeling.

2.3.1. *Tree Representation of Nonstationary Random Fields*

We use piecewise stationary fields to approximate a nonstationary one. The challenge is to find a good segmentation of the field for the approximation. With a predetermined number of layers, segmenting an image into locally stationary fields is essentially a splitting process along vertical lines at horizontal locations to capture the layers' local curvature (Fig. 8 (b)). It follows that the denser the splitting locations are, the more accurate the approximation will be.

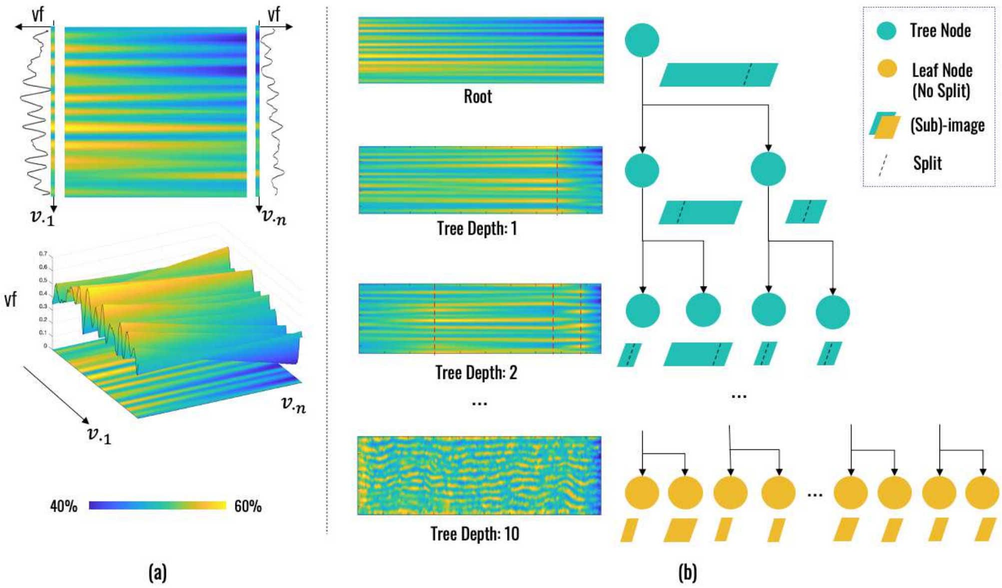

Figure 8. (a) Image interpolation from edges and (b) tree representation of cross-sectional images.

Binary tree structure is adopted to efficiently represent the splitting process, resulting in a *tree-structured random field*. A tree is a recursively structured mathematical object that contains nodes expanded from a root, and attributes attached to each node. For each cross-sectional image, we fit one binary tree, in which each root has exactly two nodes, and attach a shared splitting location along the horizontal axis to the root and the volume fractions along the left and right edges after the split to the child nodes.

To recover an image, i.e., a nonstationary field, from a tree, the segments are first reconstructed from the volume fraction information of the two edges through interpolation. Suppose an image of n (n>2) horizontal and k vertical pixels, denoted by the matrix $[v_{ij}](i = 1,2, \dots, k, j = 1,2, \dots, n)$, is to be reconstructed, and the i-th row and the j-th column of the matrix are denoted by $v_{i\cdot}$ and $v_{\cdot j}$ respectively. We have $v_{\cdot 1} = [v_{11}, v_{21}, \dots]^{\mathrm{T}}$and $v_{\cdot n} = [v_{1n}, v_{2n}, \dots]^{\mathrm{T}}$ as the volume fractions along the left and right edges. Then the interpolation operation

$$v_{\cdot\left\lceil\frac{n+1}{2}\right\rceil} \leftarrow (v_{\cdot 1} + v_{\cdot n})/2, \text{ if } n \text{ is odd,}$$
$$v_{\cdot\frac{n}{2}}, v_{\cdot\left\lceil\frac{n+2}{2}\right\rceil} \leftarrow (v_{\cdot 1} + v_{\cdot n})/2 \text{ if } n \text{ is even,} \tag{4}$$

can be executed to fill the central line(s) of an empty image based on the edges recursively (see Fig. 8(a)). The resulting image segment shows a smooth transition from $v_{i\cdot}$ to $v_{\cdot j}$, and assembling all segments from the leaf nodes of the tree yields an image of original size.

If the number of splitting locations in a tree (say s) is less than the number of horizontal pixels of the image (say n), the reconstructed image will be a smoothened version of the original data as some areas are interpolated. We define the integrated relative error (IRE) of a reconstructed image

$$IRE = \frac{\sum_x \sum_y |v_{xy}^{\text{recon}} - v_{xy}^{\text{origin}}|}{\sum_x \sum_y v_{xy}^{\text{origin}}}, \tag{5}$$

and build trees by choosing the splitting location that minimizes the IRE. The process is terminated when IRE < 0.05, realizing high quality reconstructions (see Fig. 8(b)). The tree could be viewed as a compressed representation of a nonstationary field, with its node locations summarizing the nonstationarity information.

2.3.2. *Random Resampling Tree for Distribution-free Stochastic Fiber Distribution Reconstruction*

To study the nonstationarity in the tree-structured field, first note that more splitting lines are allocated at where local curvature is observed (Fig. 9 (b)), suggesting the line's density, described by the inter-line distances, could serve as an indicator. For example, smaller distance indicates higher nonstationarity. The difference in the shapes of its distribution from individual images (examples in Fig. 9(c)) indicates sample-to-sample difference in nonstationarity. However, the grouped data, gathered from from 10 images, exhibits a converged distribution as shown in Fig. 9(d) from which we can sample and generate random trees of images.

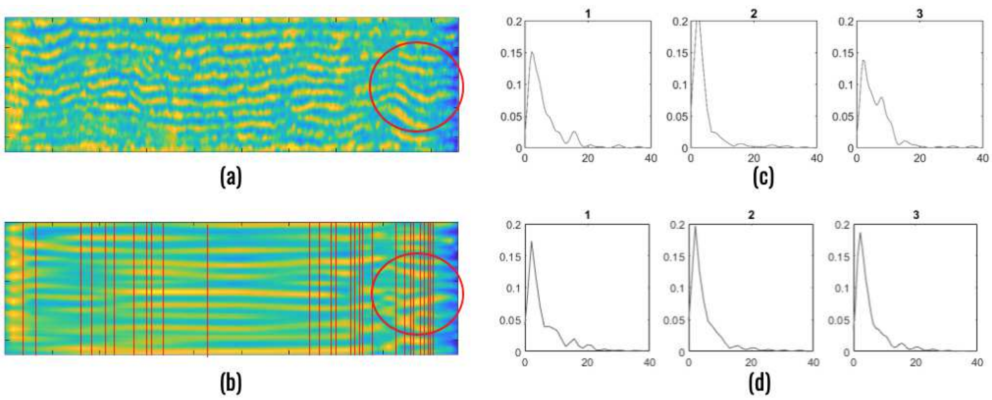

Figure 9. (a) A cross-sectional image with significant local curvature marked in circle, (b) splitting lines during tree fitting, (c) probability density estimate of inter-line distances (in pixels) from 3 individual images, and (d) density estimate of inter-line distances (in pixels) from 3 batches. Each batch contains data collected from 10 images.

A two-step algorithm is developed for generating randomly resampled trees. First, we resample from the distribution of inter-splitting-line distances (Fig. 9(d)) with replacement until the total exceeds the size of the original image. Second, volume fractions along vertical lines are resampled from existing fields, and assigned to the splitting locations from the first step, then interpolated to fill the image. Three randomly reconstructed volume fraction fields and the distribution of average volume fractions from 500 realizations are presented in Fig. 10. Compared to the original data such as Fig. 9 (a), the reconstructed images preserve the geometrical features well, such as layered structure and random curvature. We can observe from Fig. 10 (a) that the distribution of the average volume fraction (of the reconstructed images) is similar to the one from the original data. It shows that the proposed approach is capable of generating volume fraction fields that approximate the local and global features of the data, i.e. the reconstructed images mimic the real situation well.

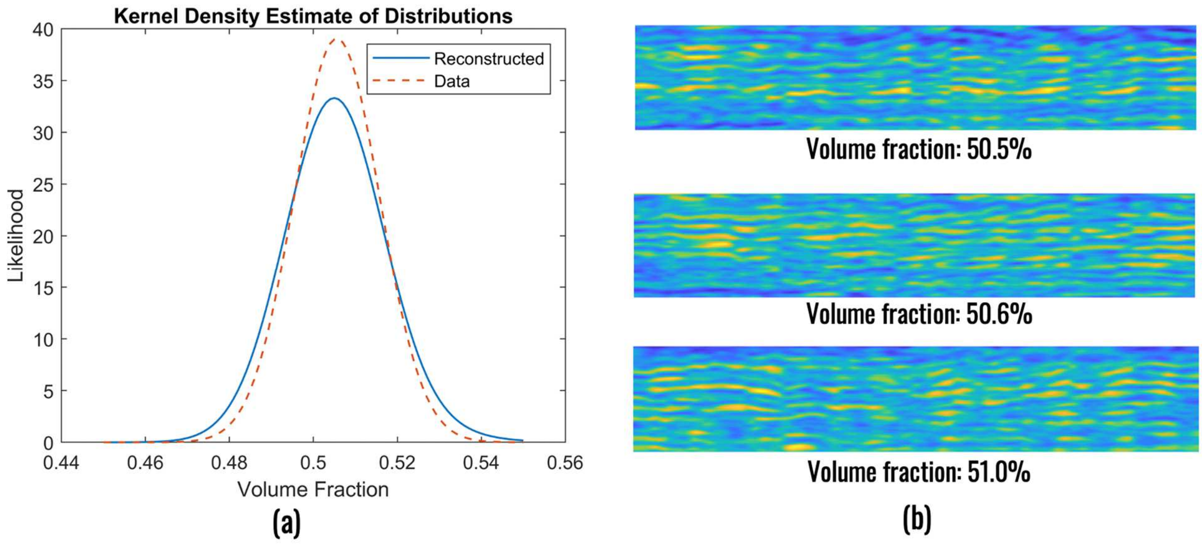

Figure 10. (a) Distribution of the volume fractions from the reconstructed cross-sectional images and (b) three examples.

2.4. *Hierarchical Conditional Sampling for Multiple Sources of Uncertainties*

If the microstructure field $\mu = \{\mu_{xyz} \in \mathbb{R}^{d_\mu} : (x, y, z) \in \mathbb{R}^3\}$ contains multiple descriptors, i.e., $d_\mu > 1$, $\mu_{xyz} = (\mu_{xyz}^{(1)}, \dots, \mu_{xyz}^{(d_\mu)})$ and $M_{xyz} = (M_{xyz}^{(1)}, \dots, M_{xyz}^{(d_\mu)})$, there is a high chance that they are correlated due to the spatial dependency in a manufacturing process. The correlation should be taken into account to construct the sampling algorithm $\mu \sim f_M(\mu)$ through

$f_M(\mu^{(1)}, \mu^{(2)}, \dots, \mu^{(d_\mu)}) =$
$f_M(\mu^{(d_\mu)} | \mu^{(d_\mu - 1)}, \dots, \mu^{(1)}) f_M(\mu^{(d_\mu - 1)} | \mu^{(d_\mu - 2)}, \dots, \mu^{(1)}) \dots f_M(\mu^{(2)} | \mu^{(1)}) f_M(\mu^{(1)})$ (subscripts omitted for cleanness). For the simplest case $d_\mu = 2$, $f_M(\mu^{(2)}, \mu^{(1)}) =$
$f_M(\mu^{(2)} | \mu^{(1)}) f_M(\mu^{(1)})$ and a *hierarchical conditional sampling* method is used to realize the fields through sampling from the first descriptor $M^{(1)}$, then the next one conditioned on it $M^{(2)} | M^{(1)}$.

For UD composites, let $\mu_{xyz} = (\alpha_{xyz}, v_{xyz})$ where α and v are the waviness angle and volume fraction. In image-based UQ, the information from characterizing a microscopic image is always conditioned on its imaging locations. For example, the waviness angles from a transverse image are $\alpha_{xyz} | y$ and the volume fractions from the cross-sectional plane is $v_{xyz} | x$. Assume all fibers share the same waviness profile, i.e., $\alpha_{xyz} | y = \alpha_x$ for all y, z, and consider volume fraction fields from two close locations $v_{xyz} | (x = x_1, \alpha = \alpha_x)$ and $v_{xyz} | (x = x_1 + \delta, \alpha = \alpha_x)$. Since the volume fractions are from the same fiber bundle with shifted distribution conditioning on α_x, they are correlated via

$$v_{xyz} \big| (x = x_1 + \delta, \alpha = \alpha_x) = v_{x[y - \tan(\alpha_x)\delta]z} \big| (x = x_1) = v_{x_1 [y - \tan(\alpha_{x_1})\delta] z}. \tag{6}$$

The $\tan(\alpha_x)\,\delta$ term reflects that the offset is proportional to the local waviness and the distance between planes. Note that Eq. (6) is a deterministic correlation if $v_{x_1 yz}$ and α_x are given. Therefore, the hierarchical conditional sampling method is accomplished by sampling from $\alpha_x = \alpha_{xyz} | y$ (Sec. 2.2) and $v_{xyz} | x = 0$ first, then obtaining all $v_{xyz} | x > 0$ through iteratively incrementing x, i.e., $v_{xyz} |\, x_i = i \cdot \delta$, using Eq. (6).

It should be noted that characterizing 3D waviness angles requires two projected local angles from $\alpha_{xyz}|y$ and $\alpha_{xyz}|z$. Due to the lack of images from both planes in our case study, we demonstrate our approaches for UD with only $\alpha_{xyz}|y$. The same approach can be applied to the other direction as wavy UD is a near-orthogonal material.

2.5. *Efficient Microstructure Reduced Order Modeling*

The challenge in UP is to reduce the computational cost of evaluating many microstructures for each simulation. A typical multiscale model uses FEA to predict the macroscale structural responses, and UD RVEs to provide the microscale material responses. At each macroscale loading step, thousands of RVEs are evaluated at all material points, each containing millions of elements and computationally burdensome through FEA. Therefore, existing UP processes are restricted to elastic analyses, where RVEs are merely used to pre-compute microstructure effective properties [11,45].

SCA is applied to reduce the RVE simulation cost for UD composites with nonlinear material responses (i.e., plasticity deformation and material damage). The UD RVEs are reconstructed with millions of voxel elements (denoted by N_E), then SCA is applied to construct reduced order models (ROMs) to accelerate their evaluation, which works by grouping all voxel elements into a limited number of clusters (denoted by $\mathrm{N_C}$, where $N_C << N_E$) based on the RVE's elastic response as illustrated in Fig. 11 and detailed in [27,29,46]. ROM significantly reduces the evaluation cost of each RVE as only N_C strain tensors are solved ($N_C << N_E$) and enhances the computational efficiency by at least four orders of magnitude , while maintains comparable accuracy of the UD responses (less than 5% difference from the direct FEA results) [29]. SCA allows UD response evaluation on-the-fly, leading to efficient multiscale simulations for UP. Details of the UD structural model are given in Section 3.2.

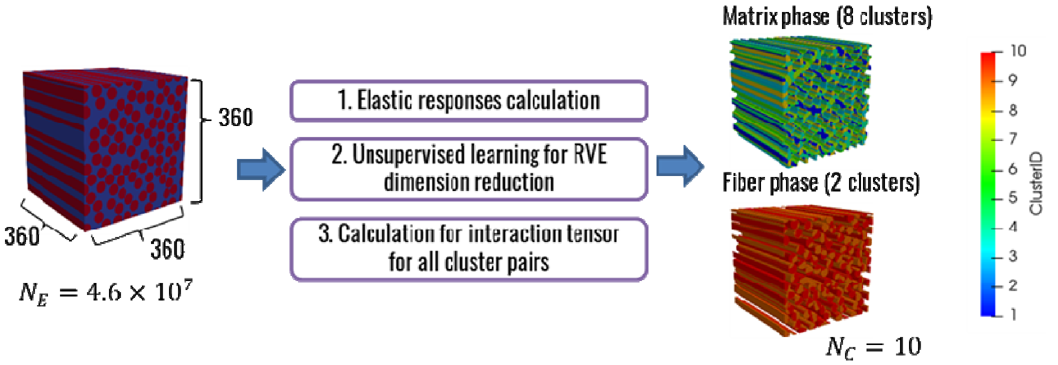

Figure 11. Three-step data compression process [28] for constructing ROM of a UD RVE: UD RVE made of 360^3 voxels with side length of 84 μm, the UD ROM contains 8 clusters in the matrix phase, and 2 clusters in the fiber phase.

2.6. *Distribution Estimates of Part Performances*

It is customary to characterize a random variable Φ by its first and second (central) moments for UQ. However, many interesting characteristics, such as nonnegativity and symmetry, cannot be determined from these low-order moments, but rather require the complete density functions $f_\Phi(\phi)$. Throughout our study, we report the estimate of $f_\Phi(\phi)$ from i.i.d. MC samples $\phi_1, \phi_2, \ldots, \phi_n$, using their *histogram* and the *kernel density estimate* (with the Gaussian kernel) [47].

Kernel-density-based permutation test [47] is chosen to determine whether the performance distribution shifts under different microstructure settings (i.e. changes in fiber waviness profiles as in Sec. 2.2.2). The null hypothesis is that the two batches of data follow the same distribution, and any permutation (e.g., randomly assign each data point to the two batches) will not introduce large differences between the two density estimates. A total of *n* permutation can be evaluated for the test statistic to obtain a p-value estimate up to $1/n$ to draw the inference regarding the null hypothesis.

3. Application to Virtual UD Compression Tests

We apply the methods in Sec. 2 for MC simulations of UD CFRP coupons under compressive loading with microstructural uncertainties. Elasto-plastic behavior of the polymer matrix is considered and a damage criterion via the local effective plastic strain is used for the FEA program. We are interested in understanding the impact of microstructural uncertainties on the variations in the plastic strain and the time to failure (TTF) simulation experiments.

3.1. *Material Models for RVE Analyses*

The elastic material constants of carbon fibers follow those in [29]. Its tensile strength, σ_{t0}, is 4200 MPa based on data provided by DowAksa, and its compressive strength is assumed to be the same. Fibers are modeled with brittle damage, governed by the stress along the longitudinal direction, i.e., a fiber fails when the absolute value of the stress exceeds σ_{t0}.

The epoxy matrix has a Young's modulus of 3.8 GPa and a Poisson's ratio ν of 0.39. The elasto-plastic hardening curve for J2 plasticity is $\bar{\sigma} = 120 - 90\exp(140\bar{\varepsilon}_p)$. The matrix ductile damage is governed by the effective plastic strain $\bar{\varepsilon}_p$. Damage indicator $d_{\text{matrix}} = 1 - \frac{\bar{\varepsilon}_{p,c}}{\bar{\varepsilon}_p}\exp(-100(\bar{\varepsilon}_p - \bar{\varepsilon}_{p,c}))$, where $\bar{\varepsilon}_{p,c} = 0.05$ is the critical effective plastic strain for damage initiation.

3.2. *Multiscale Finite Element Analysis*

To examine the impact of fiber volume fraction and waviness variations on UD laminate behavior, a UD laminate sample under compressive loading is modeled following the ASTM E2954 standard [48]. Unlike CFRP with perfectly straight fibers carrying most of the loads, it is expected that with wavy fibers, the matrix will bear increased loads due to the possible shear loading imposed. It means that the matrix material is likely to undergo plastic deformation and increases the possibility of matrix damage triggered by its damage criteria, a function of $\bar{\varepsilon}_p$. Therefore, we investigate $\bar{\varepsilon}_p$ as the key nonlinear performance measure.

The sample geometry is illustrated in Fig. 12. Its FE mesh is generated via LS-PrePost, and the FE model consists of reduced integration eight-node hexagonal element, containing one integration point per element. The boundary conditions are (1) fixed displacement (i.e., zero displacement and rotation for all degrees of freedom (DoF)) for the bottom plane, (2) *x* direction displacement allowed for the top plane, and (3) a total displacement of 1.2 mm applied on the top plane towards negative *x* direction to deform the compression sample. The "X" mark in the figure represents a material point, whose responses are computed by the UD ROM introduced in

Section 2.5. Note that replacing the original RVE with the ROM reduces system total DoF from 3.4×10^{13} to 7.6×10^{6}, providing a speedup in the order of 10^{6}. It enables multiscale UD structural analyses using a desktop workstation with multiple processors [29,42].

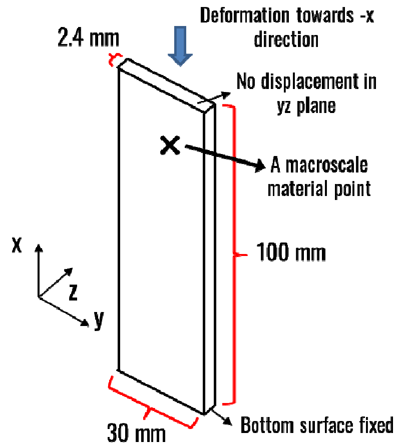

Figure 12. UD laminate compressive sample geometry: x is the fiber direction, the sample has 10 plies along the thickness direction (z direction), and the FE model contains 200×60×10 elements.

3.3. *Design of UQ Experiments*

Stochastic microstructure samples are generated via the hierarchical sampling method in Sec. 2.4. MC simulations with different waviness parameter settings are considered as in Table 1. Trial 1 is the UQ from original images, while each of Trials 2-4 has one different wave parameter compared to Trial 1. All trials have different waviness ratios (amplitude divided by wavelength), a characteristic waviness indicator as suggested by micromechanics literature such as [7]. The stochastic fiber distribution is unchanged across all trials (examples in Fig. 10). 50 simulations are conducted to ensure the convergence of resulting distributions.

Two quantities, the *maximum* $\overline{\varepsilon}_p$ and *time to failure*, are extracted from the simulation results to evaluate the part's nonlinear behavior. For each simulation, the former is a time series indexed by simulation steps which progressively increments until a variable failure time, while the latter is a discrete scalar value.

The convergence is confirmed by examining the mean and variance of the time to failure estimates via the bootstrap method. A bootstrap sample of a certain size is generated by resampling from the observed data with replacement. We estimate the variance, standard deviation, and coefficient of variations by calculating them from 10,000 bootstrap samples.

Table 1. Experiment settings.

Trial	Waviness Amplitude	Waviness Wavelength	Waviness Ratio	Number of MC Simulations
1	1x	1x	1	50
2	2x	1x	2	50
3	0.5x	1x	0.5	50
4	1x	1.25x	0.8	50

Distributions of the response of interest are reported in the subsequent section. The smooth parameter of the kernel density estimate is chosen via the Scott's rule [49] for its simplicity. To understand the microstructural uncertainty's impact on these performance indicators, we compare the distribution of the $\bar{\varepsilon}_p$ at each time step between trials. For each comparison, 1000 permutations of random data sets were conducted to compute a p-value up to a precision of 0.001.

4. Results and Discussion

UD compression simulation results under stochastic microstructures are presented in this section to demonstrate the effectiveness of the proposed UQ approaches. In Sec. 4.1, the deterministic results reveal the difference between a UQ and a pristine sample. To further understand the impact of the microstructural variability, distributions of the effective plastic strains and TTF are examined in Sec. 4.2. The influence of fiber waviness parameters is understood by comparing variable results from multiple trials in Sec. 4.3.

Fig. 13. shows the estimated time to failure and its variation (via the standard deviation) by choosing different MC sample sizes. It is evident that the estimate is steady, while the variation decreases as the sample size grows. At a sample size of 50, the coefficients of variation are 1.82%, 2.46%, 0.42%, and 0.89% for Trials 1-4. The low values, all below 3%, indicate that the

estimates of the characteristics of the stochastic quantities are subject to low variability and accurate enough for data analyses.

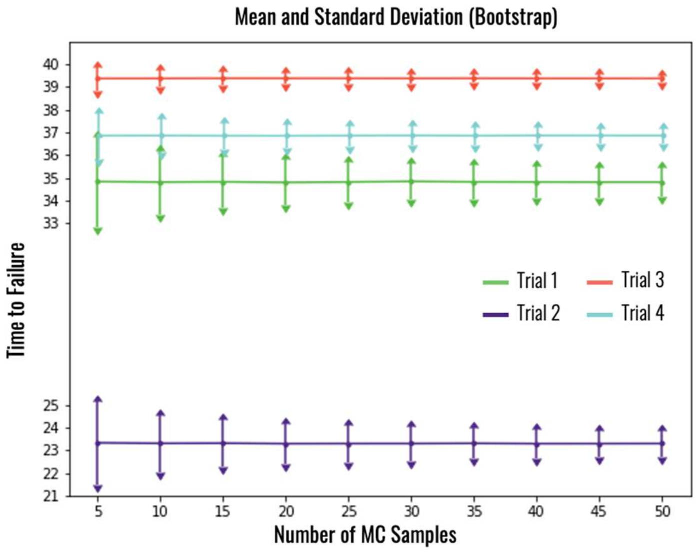

Figure 13. Bootstrap-based MC sample size convergence study of estimated time to failure. The error bars show the estimated standard deviation.

4.1. *Deterministic Multiscale Simulation*

The mechanical behavior of UD parts is predicted by the multiscale simulation. At each time step, the local constituents' stress evolution and damage initiation under the compressive loading are recorded. When the material damage intensifies and leads to RVE failure, the corresponding macroscopic element is marked as failed. Consequently, the sample loses load carrying capability. The turning point in the force versus displacement curve (example from Trial 1 in Fig. 14(a)) is used for estimating the sample failure time. Corresponding effective strain contour for the deformed compression sample at that point is shown in Fig. 14 (b), where a non-uniform effective strain distribution is observed due to fiber waviness and nonuniform distribution. Those regions with significantly higher effective strain magnitude are more prone to failure.

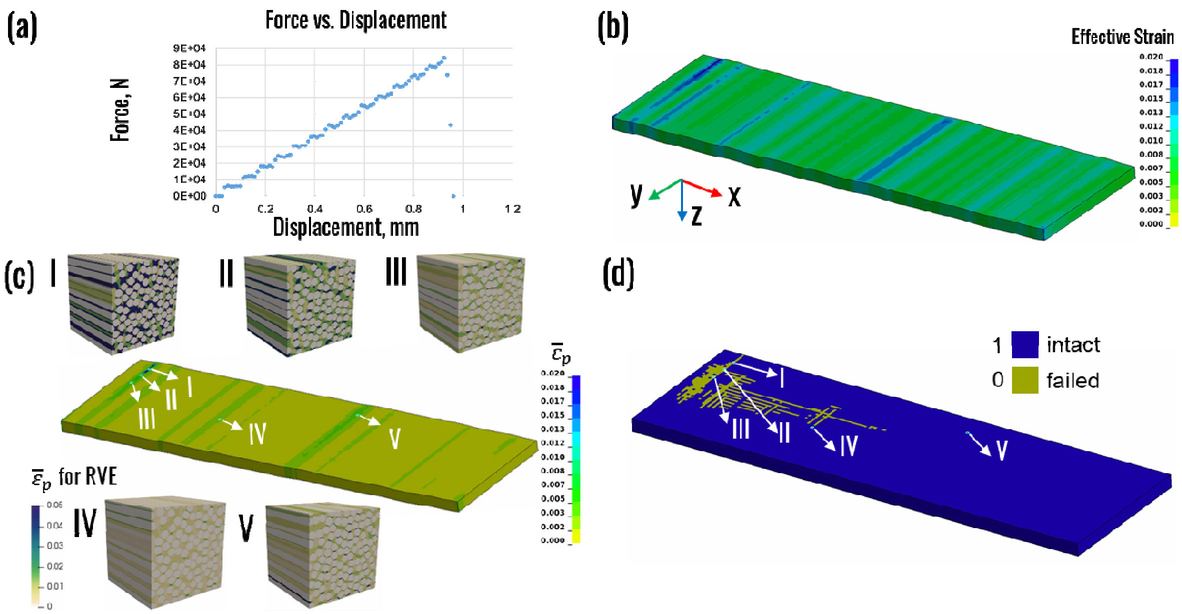

Figure 14. (a) Force vs. displacement curve for one realization in Trial 1; (b) Effective strain contour of the compression sample illustrated using LS-PrePost; (c) $\overline{\varepsilon}_p$ contour of the compression sample at displacement of 0.93 mm with five locations (I to V) marked and corresponding UD RVE at each location; and (d) Compression sample (in undeformed configuration) element-wise failure indicator at displacement of 0.96 mm.

Microstructure evolution is analyzed to understand the root cause of failure in the compression sample. First, $\overline{\varepsilon}_p$ contour is plotted for the compression sample in Fig. 14 (c), where $\overline{\varepsilon}_p$ at each material point is homogenized from the UD RVE. The maximum $\overline{\varepsilon}_p$ is observed at location *I*, and the underneath UD RVE ($V_f = 52\%$) $\overline{\varepsilon}_p$ contour at location *I* is visualized in Fig. 14 (c). All fibers are intact and no $\overline{\varepsilon}_p$ is observed there due to their brittleness. Meanwhile, the matrix phase shows significant $\overline{\varepsilon}_p$ accumulation whose magnitude exceeds the critical value of 0.05. Therefore, the matrix phase begins to degrade at location *I*, leading to the loss of load carry capacity of that RVE. This is the cause of compression sample failure at the turning point in Fig 13 (a) (0.93 mm).

In addition to capturing the cause of failure, our methodology provides insights into failure pattern in the sample after failure initiation at *I*. In Fig. 14 (c), observing the RVEs at *II* ($V_f = 49\%$) and *III* ($V_f = 53\%$), the contours show $\overline{\varepsilon}_p$ has reached the critical value of 0.05 in the matrix region, indicating that the possible failure pattern would be along the *y* direction, across *I*,

II and III. On the contrary, RVEs at IV ($V_f = 52\%$) and V ($V_f = 57\%$) show lower $\bar{\varepsilon}_p$ magnitude. It suggests IV and V are less susceptible to failure, which is further verified by the binary element-wise failure contour of the sample (Fig. 14 (d)), where I, II and III are marked as failure, and IV and V are marked as intact. Another interesting observation unveiled by Figs. 13 (c) and (d) is that despite RVEs at I, II, and III have different fiber volume fractions, they show similar magnitude of $\bar{\varepsilon}_p$ as three RVEs have the same fiber orientation. It suggests for a UD compression sample, fiber waviness plays a more important role than fiber volume fraction in governing the sample structural performance.

4.2. *Stochastic Nonlinear Behavior from Image-based Microstructural Uncertainty*

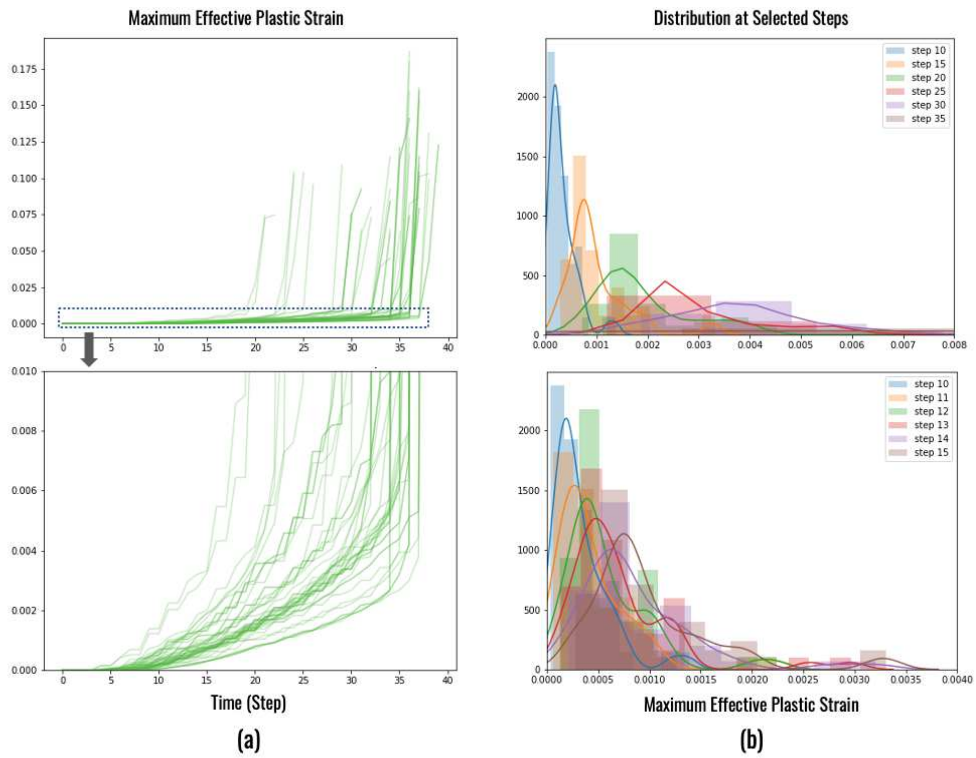

Figure 15. Stepwise maximum effective plastic strain for Trial 1: (a) overall (upper) and zoomed-in view (lower) of the response curve and (b) distributions of the response every 5 steps (upper) and every step between steps 10 and 15 (lower).

The FEA analysis suggests that samples under compression fail where the maximum $\bar{\varepsilon}_p$ resides. Therefore, stochastic analysis is performed to investigate the uncertainty in the maximum $\bar{\varepsilon}_p$ per loading step, which is proportional to the displacement.

Fig. 15 shows the ensemble of the distributions of maximum effective plastic strain at each step from Trial 1 (same waviness amplitude and wavelength as in microscopic images). Notable variations can be observed at each step under the microstructure uncertainty. The increasing width of the distributions shows the rising impact of uncertainty as the nonlinear behavior becomes dominant.

The distribution of TTF is presented in Fig. 16 (a). The histogram shows a range of TTF between steps 22 and 40, and through the kernel density estimate it is clear that the distribution is non-Gaussian and left-skewed. The density function is related to the observed failure rate over time through the cumulative distribution function of TTF, $F_\Phi(s) = \int_{-\infty}^{s} \tilde{f}_\Phi(\phi) \mathrm{d}\phi$. Such a curve as shown in Fig. 16 (b) provides a measure of the time dependent reliability, i.e., probability of failure, of a part under the microstructure variability.

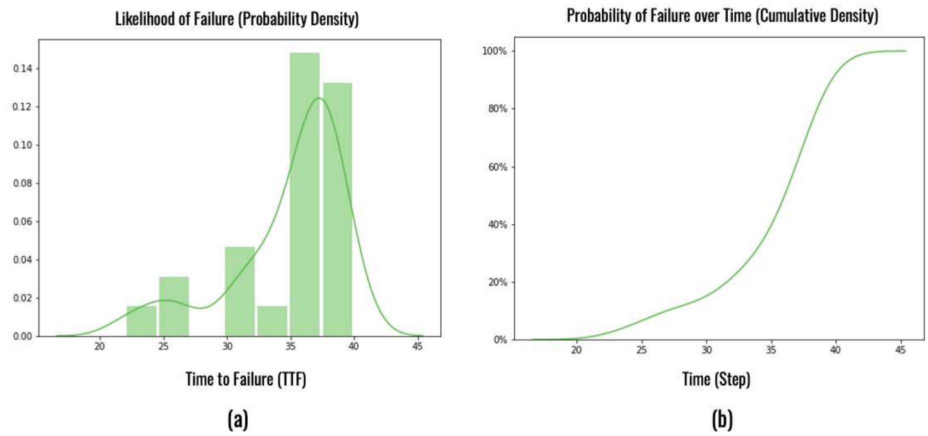

Figure 16. (a) Probability density of the TTF and (b) cumulative density as the probability of failure over time.

4.3. *Influence of Fiber Waviness*

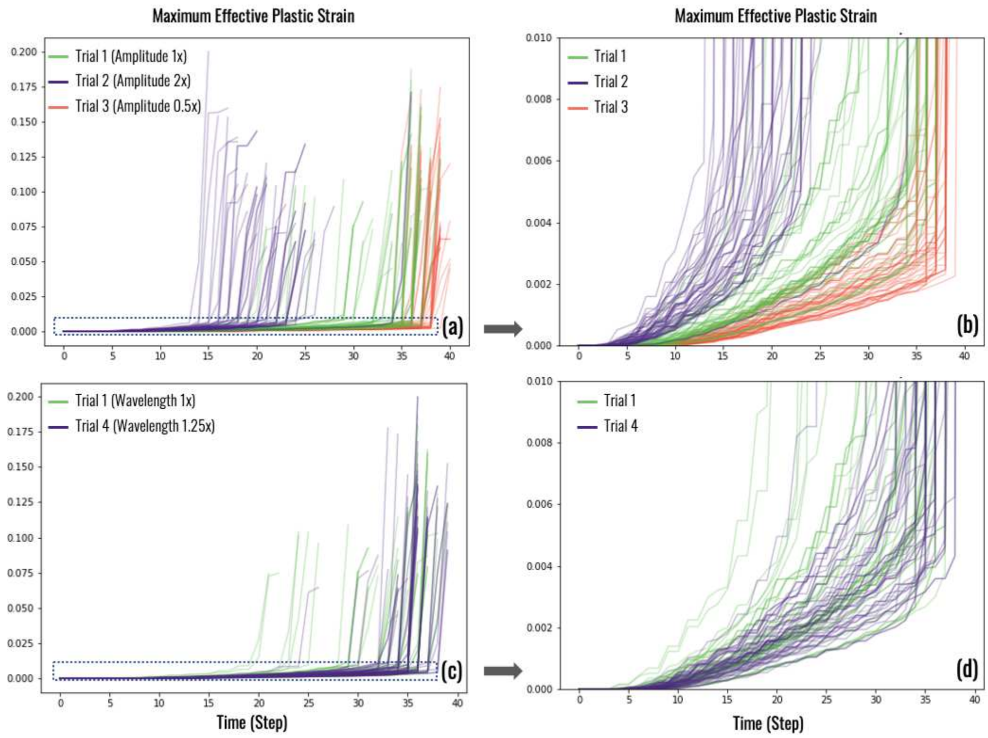

Figure 17. Stepwise maximum effective plastic strain for Trial 1-4: (a) and (b) are overview and zoomed-in views for Trials 1-3 and (c) and (d) are those plots for Trials 1 and 4.

The maximum $\bar{\varepsilon}_p$ is a local measure of progress to failure. Figs. 16 (a) and (b), in Trials 1-3 marked with different colors, exhibit significant distinction in the stochastic responses. At any time, larger amplitude leads to generally degraded performance, i.e., higher local plastic strain and earlier failure, which is also in line with the experimental and simulation results for other property indicators [5,7,35]. However, for Trials 1 and 4, although the waviness ratio is different, the resulting curves overlap and the distributions are not notably different. P-values of the permutation tests, quantifying the dissimilarity, are plotted in Fig. 18. A low p-value (e.g., $p <$ 0.05) suggests a strong evidence against the hypothesis that the distributions are similar.

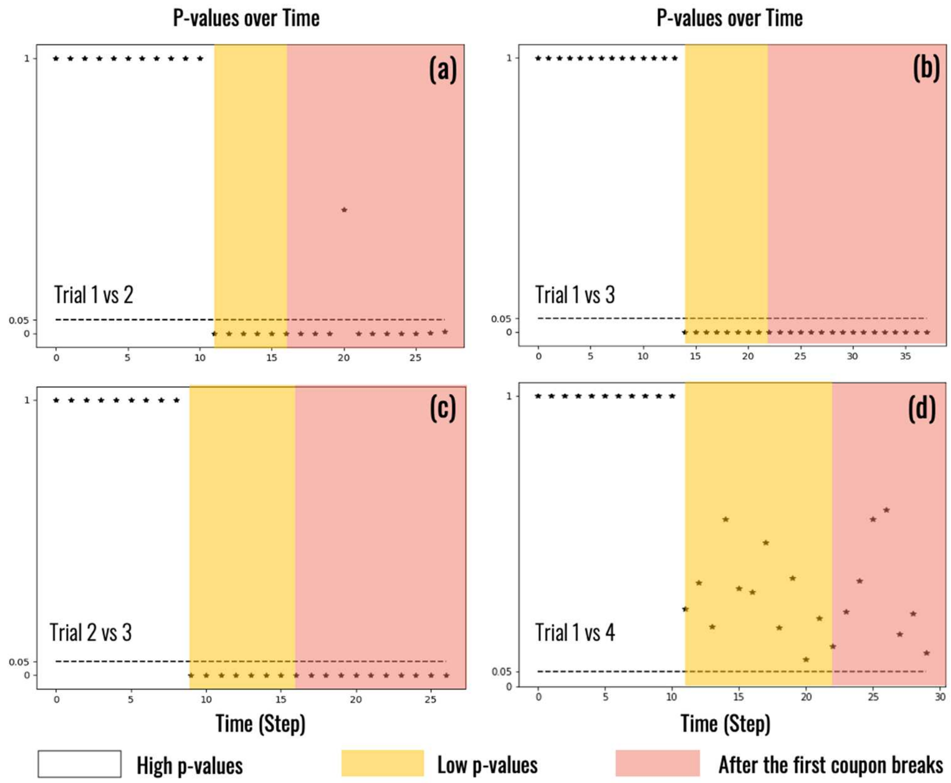

Figure 18. Stepwise P-values by comparing (a) Trials 1 and 2, (b) Trials 1 and 3, (c) Trials 2 and 3, and (d) Trials 1 and 4.

High p-values are observed for the first several steps, indicating if the applied deformation is small, the distribution of the nonlinear responses does not differ significantly even when the amplitude of fiber waviness is doubled (i.e., Trials 1 versus 2, 1 versus 3) or quadrupled (i.e., Trial 2 versus 3). However, after a certain time step, the p-value drops to below 0.05 and maintains at a low level. Therefore, there is a critical time after which the distributions are distinguishable from each other corresponding to different magnitudes of waviness amplitude. On the other hand, Fig. 18 (d) reveals that a drop of waviness ratio from 1 to 0.8 through increasing the wavelength does not lead to statistically significant distinction between the local strain readings.

The difference between the distributions of TTF is more evident (see Fig. 19 (a) and (b)). P-values from 5000 permutations for the pairwise comparisons are listed in Table 2. Although the high significance levels from pairwise comparisons among the first three trials are not surprising *per se*, it is worth mentioning that under microstructural uncertainties, distinguishable distributions of responses can be obtained by altering fiber waviness parameters. The uncertainties in microstructure, nonlinear behavior, and TTF can be statistically linked and form a causality chain. However, similarly to Fig. 18 (d), Fig. 19 (c) and (d) together with the last row in Table 2 indicates that the stochastic performance will not show significant difference if the waviness shape tuning is insufficient.

Three stages with distinct uncertainty patterns can be identified as the loading increments (Fig. 18). The initial stage is microstructure-insensitive where the nonlinear local responses are all close to zero and distributed similarly. It is followed by a characteristic period in which the distribution is specific to the microstructure configuration, as they are mutually different under different microstructures. Finally, the parts start to fail with distinctive probability distributions (Fig. 19 (a)). Note that the second stage is vital as the distributions in this period are the result of the microstructure and are indicative of the TTF distribution. This UQ capability has profound implications because based on the profile of characteristic stages, we can infer when the parts fail while they are still safe during current period. Such characteristic stages cannot be derived without explicitly quantifying microstructural uncertainty, as they are identified through comparing the distributions of the performance.

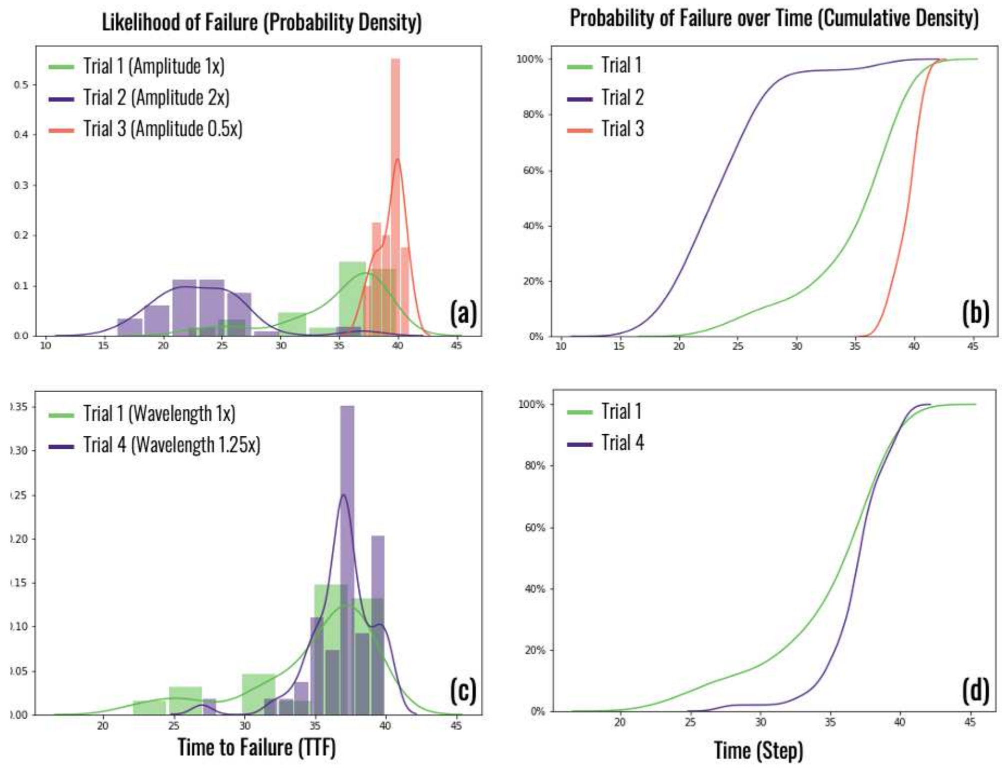

Figure 19. (a) Probability density of the TTF for Trials 1-3, (b) cumulative density as the probability of failure over time for Trials 1-3, (c) and (d) are the same plots for Trials 1 and 4.

Table 2. P-values from comparisons of TTF between trials.

Comparison	P-value
Trials 1 vs. 2	< 0.001
Trials 1 vs. 3	< 0.001
Trials 2 vs. 3	< 0.001
Trials 1 vs. 4	0.1264

It should be noted that data quality is crucial in generating MC microstructure samples. The distribution-free sampling algorithms can generate realistic samples, but any contamination of the data, such as characterization error, will also be reproduced. Therefore, the resulting quantified uncertainty is the compound effect of (1) the stochasticity of microstructures, (2) the integrity of the image data, and (3) the prediction uncertainty of the numerical models. We assume (2) and (3) are small, and (1) is the focus throughout the paper.

5. Conclusion

A microscopic-images-based UQ framework is established to addresses three fundamental challenges in UQ of fiber composites with complex microstructural variabilities: (1) microstructure information extraction, (2) multi-source dependent microstructure uncertainty modeling and sampling, and (3) efficient uncertainty propagation to stochastic nonlinear performance. Our methodological contributions include:

(1) development of image characterization and stochastic reconstruction algorithms for modeling complex microstructural variability, including the linear texture regression with frequency domain sampling and tree-structured nonstationary random fields, with a distribution-free construction suitable when the parametric distributions are difficult to derive;
(2) use of a hierarchical conditional sampling method to generate 3D random fields with multiple correlated sources of uncertainties, including fiber waviness and distribution for UQ of UD composites; and
(3) application of multiscale simulations with reduced order modeling techniques to enable efficient propagation of microstructure uncertainties to nonlinear part performance and failure behavior.

The UQ results suggest that the microstructural uncertainties have an increasing impact on the nonlinear mechanical responses when the loading increases. A three-stage characterization of the stochastic responses is identified consisting of an initial microstructure-insensitive stage, a characteristic stage where the distribution of the response can imply the magnitude of microstructure variability and indicate when the parts fail, and finally the failure stage. We also observed that small perturbations of the microstructure (e.g., waviness ratio) lead to statistically equivalent results, showing UD CFRP's robustness to small microstructure change. Our future work includes using experimental results to validate the simulations, utilizing our understanding of the relationship between stochastic microstructure and uncertain performance to infer the microstructure variability in new samples from performance measurement data, and predict their time-dependent failure probability.

Acknowledgement

This work was sub-contracted from Ford Motor Company which has received the award from US Department of Energy (Award Number: DE-EE0006867). Support from AFOSR (FA9550-18-1-0381), Center for Hierarchical Materials Design (ChiMaD NIST 70NANB19H005), Northwestern University's Predictive Science and Engineering Design (PS&ED) Cluster are also acknowledged. The authors would like to Dr. Yang Li for assistance with preparing the image samples.

Data Availability

The raw and processed data required to reproduce these findings are available to download from http://dx.doi.org/10.17632/nvkxx7nphg.1.

References

[1] Concil NR. Integrated computational materials engineering: a transformational discipline for improved competitiveness and national security. National Academies Press; 2008.

[2] Zhang W, Ren H, Wang Z, Liu WK, Chen W, Zeng D, et al. An integrated computational materials engineering method for woven carbon fiber composites preforming process. AIP Conf. Proc., vol. 1769, 2016, p. 170036.

[3] Liu KC, Ghoshal A. Validity of random microstructures simulation in fiber-reinforced composite materials. Compos Part B Eng 2014;57:56–70. https://doi.org/10.1016/j.compositesb.2013.08.006.

[4] Thomas M, Boyard N, Perez L, Jarny Y, Delaunay D. Representative volume element of anisotropic unidirectional carbon-epoxy composite with high-fibre volume fraction. Compos Sci Technol 2008;68:3184–92. https://doi.org/10.1016/j.compscitech.2008.07.015.

[5] Altmann A, Gesell P, Drechsler K. Strength prediction of ply waviness in composite materials considering matrix dominated effects. Compos Struct 2015;127:51–9. https://doi.org/10.1016/J.COMPSTRUCT.2015.02.024.

[6] Karami G, Garnich M. Micromechanical study of thermoelastic behavior of composites with periodic fiber waviness. Compos Part B Eng 2005;36:241–8. https://doi.org/10.1016/J.COMPOSITESB.2004.09.005.

[7] Hsiao HM, Daniel IM. Elastic properties of composites with fiber waviness. Compos Part A Appl Sci Manuf 1996;27:931–40. https://doi.org/10.1016/1359-835X(96)00034-6.

[8] Sriramula S, Chryssanthopoulos MK. Quantification of uncertainty modelling in stochastic analysis of FRP composites. Compos Part A Appl Sci Manuf 2009;40:1673–84. https://doi.org/https://doi.org/10.1016/j.compositesa.2009.08.020.

[9] Lekou DJ, Philippidis TP. Mechanical property variability in FRP laminates and its effect on failure prediction. Compos Part B Eng 2008;39:1247–56.

https://doi.org/10.1016/j.compositesb.2008.01.004.

[10] Sasikumar P, Suresh R, Gupta S. Stochastic model order reduction in uncertainty quantification of composite structures. Compos Struct 2015;128:21–34. https://doi.org/https://doi.org/10.1016/j.compstruct.2015.03.045.

[11] Bostanabad R, Liang B, Gao J, Liu WK, Cao J, Zeng D, et al. Uncertainty quantification in multiscale simulation of woven fiber composites. Comput Methods Appl Mech Eng 2018;338:506–32. https://doi.org/10.1016/J.CMA.2018.04.024.

[12] Dey S, Mukhopadhyay T, Adhikari S. Uncertainty quantification in laminated composites: A meta-model based approach. CRC Press; 2018.

[13] Naskar S, Mukhopadhyay T, Sriramula S, Adhikari S. Stochastic natural frequency analysis of damaged thin-walled laminated composite beams with uncertainty in micromechanical properties. Compos Struct 2017;160:312–34. https://doi.org/10.1016/j.compstruct.2016.10.035.

[14] Ilyani Akmar ABB, Lahmer T, Bordas SPAPA, Beex LAAAA, Rabczuk T. Uncertainty quantification of dry woven fabrics: A sensitivity analysis on material properties. Compos Struct 2014;116:1–17. https://doi.org/https://doi.org/10.1016/j.compstruct.2014.04.014.

[15] Scarth C, Cooper JE, Weaver PM, Silva GHC. Uncertainty quantification of aeroelastic stability of composite plate wings using lamination parameters. Compos Struct 2014;116:84–93. https://doi.org/10.1016/j.compstruct.2014.05.007.

[16] Liu WK, Belytschko T, Mani A. Random field finite elements. Int J Numer Methods Eng 1986;23:1831–45. https://doi.org/10.1002/nme.1620231004.

[17] Liu WK, Belytschko T, Mani A. Probabilistic finite elements for nonlinear structural dynamics. Comput Methods Appl Mech Eng 1986;56:61–81. https://doi.org/10.1016/0045-7825(86)90136-2.

[18] Liu WK, Besterfield G, Belytschko T. Transient probabilistic systems. Comput Methods Appl Mech Eng 1988;67:27–54. https://doi.org/10.1016/0045-7825(88)90067-9.

[19] Liu WK, Besterfield GH, Belytschko T. Variational Approach to Probabilistic Finite Elements. J Eng Mech 1988;114:2115–33. https://doi.org/10.1061/(ASCE)0733-9399(1988)114:12(2115).

[20] Ghanem RG, Spanos PD. Stochastic Finite Elements: A Spectral Approach. Springer New York; 1991. https://doi.org/10.1007/978-1-4612-3094-6.

[21] Thapa M, Mulani SB, Walters RW. Stochastic multi-scale modeling of carbon fiber reinforced composites with polynomial chaos. Compos Struct 2019;213:82–97. https://doi.org/10.1016/j.compstruct.2019.01.068.

[22] Shi D, Teng X, Jing X, Lyu S, Yang X. A multi-scale stochastic model for damage analysis and performance dispersion study of a 2.5D fiber-reinforced ceramic matrix composites. Compos Struct 2020;248:112549. https://doi.org/10.1016/j.compstruct.2020.112549.

[23] Naskar S, Mukhopadhyay T, Sriramula S, Adhikari S. Stochastic natural frequency analysis of damaged thin-walled laminated composite beams with uncertainty in micromechanical properties. Compos Struct 2017;160:312–34. https://doi.org/https://doi.org/10.1016/j.compstruct.2016.10.035.

[24] Cheng H, Gao J, Kafka OL, Zhang K, Luo B, Liu WK. A micro-scale cutting model for UD CFRP composites with thermo-mechanical coupling. Compos Sci Technol 2017;153:18–31.

[25] Lutif J. Computational micromechanics modeling of damage-dependent bituminous composites based on two-way coupled multiscale approach 2011.

[26] Chinesta F, Cueto E, Abisset-Chavanne E, Duval JL, El Khaldi F. Virtual, digital and hybrid twins: a new paradigm in data-based engineering and engineered data. Arch Comput Methods Eng 2018:1–30.

[27] Liu Z, Bessa MA, Liu WK. Self-consistent clustering analysis: an efficient multi-scale scheme for inelastic heterogeneous materials. Comput Methods Appl Mech Eng 2016;306:319–41.

[28] Liu Z, Fleming M, Liu WK. Microstructural material database for self-consistent clustering analysis of elastoplastic strain softening materials. Comput Methods Appl Mech Eng 2018;330:547–77.

[29] Gao J, Shakoor M, Domel G, Merzkirch M, Zhou G, Zeng D, et al. Predictive multiscale modeling for Unidirectional Carbon Fiber Reinforced Polymers. Compos Sci Technol 2020;186:107922.

[30] Sabuncuoglu B, Tanabi H, Soete J, Lomov S V. Micro-CT analysis of deviations in fiber orientation and composite stiffness near the microvascular channels embedded in glass-fiber reinforced composites. Compos Struct 2020;237:111896. https://doi.org/10.1016/j.compstruct.2020.111896.

[31] Wu L, Chung CN, Major Z, Adam L, Noels L. From SEM images to elastic responses: A stochastic multiscale analysis of UD fiber reinforced composites. Compos Struct 2018;189:206–27. https://doi.org/10.1016/j.compstruct.2018.01.051.

[32] Chun H-J, Shin J-Y, Daniel IM. Effects of material and geometric nonlinearities on the tensile and compressive behavior of composite materials with fiber waviness. Compos Sci Technol 2001;61:125–34. https://doi.org/10.1016/S0266-3538(00)00201-3.

[33] Wu C, Gu Y, Luo L, Xu P, Wang S, Li M, et al. Influences of in-plane and out-of-plane fiber waviness on mechanical properties of carbon fiber composite laminate. J Reinf Plast Compos 2018;37:877–91. https://doi.org/10.1177/0731684418765981.

[34] Garnich MR, Karami G. Localized Fiber Waviness and Implications for Failure in Unidirectional Composites. J Compos Mater 2005;39:1225–45. https://doi.org/10.1177/0021998305048748.

[35] Hsiao HM, Daniel IM. Nonlinear Elastic Behavior of Unidirectional Composites With Fiber Waviness Under Compressive Loading. J Eng Mater Technol 1996;118:561–70.

[36] Buryachenko VA, Pagano NJ, Kim RY, Spowart JE. Quantitative description and numerical simulation of random microstructures of composites and their effective elastic moduli. Int J Solids Struct 2003;40:47–72. https://doi.org/10.1016/S0020-7683(02)00462-6.

[37] Ghosh S, Nowak Z, Lee K. Quantitative characterization and modeling of composite microstructures by Voronoi cells. Acta Mater 1997;45:2215–34. https://doi.org/10.1016/S1359-6454(96)00365-5.

[38] Pyrz R. Quantitative description of the microstructure of composites. Part I: Morphology of unidirectional composite systems. Compos Sci Technol 1994;50:197–208. https://doi.org/10.1016/0266-3538(94)90141-4.

[39] YANG S, TEWARI A, GOKHALE AM. Modeling of non-uniform spatial arrangement of fibers in a ceramic matrix composite. Acta Mater 1997;45:3059–69. https://doi.org/10.1016/S1359-6454(96)00394-1.

[40] Pyrz R. Correlation of microstructure variability and local stress field in two-phase materials. Mater Sci Eng A 1994;177:253–9. https://doi.org/10.1016/0921-5093(94)90497-9.

[41] Shan Z, Gokhale AM. Representative volume element for non-uniform micro-structure. Comput Mater Sci 2002;24:361–79. https://doi.org/10.1016/S0927-0256(01)00257-9.

[42] Li H, Kafka OL, Gao J, Yu C, Nie Y, Zhang L, et al. Clustering discretization methods for generation of material performance databases in machine learning and design optimization. Comput Mech 2019;64:281–305. https://doi.org/10.1007/s00466-019-01716-0.

[43] Bostanabad R, Chen W, Apley DW. Characterization and reconstruction of 3D stochastic microstructures via supervised learning. J Microsc 2016;264:282–97. https://doi.org/10.1111/jmi.12441.

[44] Brockwell PJ, Davis RA, Fienberg SE. Time Series: Theory and Methods: Theory and Methods. Springer Science & Business Media; 1991.

[45] Liang B, Zhang W, Fenner JS, Gao J, Shi Y, Zeng D, et al. Multi-scale modeling of mechanical behavior of cured woven textile composites accounting for the influence of yarn angle variation. Compos Part A Appl Sci Manuf 2019;124:105460. https://doi.org/10.1016/j.compositesa.2019.05.028.

[46] Han X, Gao J, Fleming M, Xu C, Xie W, Meng S, et al. Efficient multiscale modeling for woven composites based on self-consistent clustering analysis. Comput Methods Appl Mech Eng 2020;364:112929. https://doi.org/10.1016/j.cma.2020.112929.

[47] Bowman AW, Azzalini A. Applied smoothing techniques for data analysis : the kernel approach with S-Plus illustrations. Clarendon Press; 1997.

[48] ASTM. Standard Test Method for Axial Compression Test of Reinforced Plastic and Polymer Matrix Composite Vertical Members 1. vol. i. 2015. https://doi.org/10.1520/E2954-15.

[49] Scott DW. Multivariate Density Estimation : Theory, Practice, and Visualization. Wiley; 2015.